3-30-2018

Highly Efficient Electrochemical Reforming of CH_4/CO_2 in a Solid Oxide Electrolyser

Jinhai Lu

Changli Zhu

Changchang Pan

Wenlie Lin

John P. Lemmon

See next page for additional authors

Publication Info

Published in *Electrochemistry*, Volume 4, Issue 3, 2018.

ELECTROCHEMISTRY

Highly efficient electrochemical reforming of CH_4/CO_2 in a solid oxide electrolyser

Jinhai Lu,[1] Changli Zhu,[1] Changchang Pan,[1] Wenlie Lin,[2] John P. Lemmon,[3] Fanglin Chen,[4] Chunsen Li,[2] Kui Xie[1]*

Reforming CH_4 into syngas using CO_2 remains a fundamental challenge due to carbon deposition and nanocatalyst instability. We, for the first time, demonstrate highly efficient electrochemical reforming of CH_4/CO_2 to produce syngas in a solid oxide electrolyser with CO_2 electrolysis in the cathode and CH_4 oxidation in the anode. In situ exsolution of an anchored metal/oxide interface on perovskite electrode delivers remarkably enhanced coking resistance and catalyst stability. In situ Fourier transform infrared characterizations combined with first principle calculations disclose the interface activation of CO_2 at a transition state between a CO_2 molecule and a carbonate ion. Carbon removal at the interfaces is highly favorable with electrochemically provided oxygen species, even in the presence of H_2 or H_2O. This novel strategy provides optimal performance with no obvious degradation after 300 hours of high-temperature operation and 10 redox cycles, suggesting a reliable process for conversion of CH_4 into syngas using CO_2.

INTRODUCTION

CO_2 and CH_4 are important contributors to the greenhouse effect, as well as cheap and nontoxic building blocks for current single-carbon source chemistry (*1*). Conversion of CH_4 into syngas using CO_2 not only provides the key feedstock for Fischer-Tropsch synthesis but also contributes to the mitigation of greenhouse gases. The dry reforming of CH_4 with CO_2, an endothermic reaction ($CO_2 + CH_4 = 2CO + 2H_2$), is particularly interesting from an economic point of view and has long been considered as a viable method to convert CH_4 into syngas. However, carbon deposition, which mainly originates from CO disproportionation and CH_4 pyrolysis, causes severe deactivation of non-noble metal catalysts like nickel (*2*, *3*). Long-term stability of nanocatalysts at high temperatures remains another major challenge due to nanoparticle agglomeration leading to performance degradation (*4*, *5*). In terms of mechanism, the dry reforming of CH_4 with CO_2 mainly proceeds with CH_4 dehydrogenation/oxygenation and decomposition of CO_2 to CO in a thermal catalysis process. In addition, this reaction would be ideally realized in an efficient electrochemical process by combining CO_2 electrolysis ($CO_2 + 2e^- = CO + O^{2-}$) with electrochemical oxidation of CH_4 ($CH_4 + O^{2-} = CO + 2H_2 + 2e^-$) in a simultaneous process.

Solid oxide electrolysers (SOEs) as the key technology of CO_2 electrolysis have been attracting great interest because of their high efficiencies in producing low-carbon fuels from renewable electrical energy (*6*, *7*). The advantages of long life, flexible scale, and low cost have demonstrated huge practical application potentials. They can exploit available high-temperature exhaust heat to maximize electrical energy efficiency, and the high operation temperature of around 800° to 1000°C well fits the requirement of the dry reforming of CH_4 with CO_2 to generate syngas. In an oxide ion–conducting SOE, CO_2 gas can be directly electrolyzed into CO and O^{2-} ($CO_2 + 2e^- = CO + O^{2-}$) at the cathode, while the generated O^{2-} ions travel through the electrolyte to the anode to form O_2 gas ($O^{2-} - 2e^- = 1/2O_2$), under an externally applied potential. This unique mechanism provides the possibility of direct utilization of O^{2-} to in situ electrochemically oxidize CH_4 ($CH_4 + O^{2-} = CO + 2H_2 + 2e^-$) into syngas in the anode. In this case, the electrochemical reforming of CH_4/CO_2 with CO_2 reduction in the cathode and CH_4 oxidation in the anode may be achieved through an efficient electrochemical process, which would demonstrate huge economic and sustainability potential when exploiting available exhaust heat streams and renewable electrical energy.

Electrochemical reforming of CH_4/CO_2 in an SOE involves the electrolysis of CO_2 in the cathode and the electrochemical oxidation of CH_4 in the anode in a simultaneous process. The CO disproportionation and CH_4 pyrolysis may be mainly distributed on the cathode and anode, respectively, which may accordingly relieve the severe carbon deposition that is commonly observed in the dry reforming of CH_4 with CO_2 on a metal catalyst. In addition, the electrochemical pump of oxygen species to the anode would facilitate the removal and oxidation of deposited carbon on the porous electrode scaffold (*8*). Here, we use redox-stable perovskite-type $La_{0.75}Sr_{0.25}Cr_{0.5}Mn_{0.5}O_{3-\delta}$ (LSCM) both as cathode and anode to assemble a symmetric cell for electrochemical reforming of CH_4/CO_2. Ceramic LSCM is a mixed conductor with very high oxygen storage capacity and has already demonstrated excellent coking resistance for CH_4 reforming and oxidation (*9*, *10*). In addition, LSCM has been confirmed to be an excellent coking-resistant cathode for CO_2 electrolysis with long-term stability being observed during high-temperature operation (*11*, *12*). However, the performance of these ceramic electrodes is still limited by insufficient electrocatalytic activity, although it can be substantially enhanced by loading metal nanocatalyst to create sufficient active interfaces.

The incorporation of catalytic Ni nanoparticles has already been proved to be an effective approach to enhance catalytic activity for CO_2 dry reforming of CH_4. However, long-term instability of the nanocatalysts remains a major challenge due to nanocatalyst agglomeration leading to catalysis performance degradation at high temperatures (*13*). An alternative method is to dope the metal in the host lattice of LSCM when preparing the catalyst in air, which is then exsolved in the form of metallic nanoparticles at the surface of an LSCM scaffold under reducing conditions. In this way, the metal nanoparticles can be grown in situ and

[1]Key Laboratory of Design and Assembly of Functional Nanostructures, Fujian Institute of Research on the Structure of Matter, Chinese Academy of Sciences, Fuzhou, Fujian 350002, China. [2]State Key Laboratory of Structure Chemistry, Fujian Institute of Research on the Structure of Matter, Chinese Academy of Sciences, Fuzhou, Fujian 350002, China. [3]National Institute of Clean and Low-Carbon Energy, Beijing 102211, China. [4]Department of Mechanical Engineering, University of South Carolina, 300 Main Street, Columbia, SC 29208, USA.
*Corresponding author. Email: kxie@fjirsm.ac.cn

anchored on the LSCM surface if the conditions are carefully chosen to avoid full decomposition. In this case, any possible agglomeration of exsolved metal nanoparticles on the substrate can be remedied by periodically cycling from oxidizing to reducing conditions. The in situ growth of metal nanoparticles directly from a perovskite backbone support particularly exhibits enhanced high-temperature stability and coking resistance for CO_2 electrolysis due to the stronger metal/oxide interactions resulting from anchored interface architectures at the nanoscale (*14*). An additional way of improving catalytic performance with coking resistance is formation of alloy nanoparticles between Ni and other metals. This alloy catalyst with intimate interaction between different metals delivers excellent performance both for catalytic activity and coking resistance for the dry reforming of CH_4 with CO_2 (*15*). It is therefore proposed that a highly efficient electrochemical reforming of CH_4/CO_2 with remarkable coking resistance and long-term stability would be anticipated when using a perovskite LSCM electrode scaffold with in situ exsolution of alloy nanocatalysts in an SOE. The $Ni_{1-x}Cu_x$ alloys in the interface architectures are expected to deliver strong interface interactions that highly favor CO_2 electrolysis in the cathode and CH_4 oxidation in the anode. Copper has a lower selectivity toward H_2 evolution, but it has excellent CO_2/CO adsorption properties and coking resistance (*16*, *17*). In contrast, Ni has high catalytic activity but tends to be prone to high coke formation (*18*). We therefore take a compromise approach by in situ forming $Ni_{1-x}Cu_x$ alloys in the interface architectures and using the respective catalysis characteristics of both nickel and copper.

Here, we, for the first time, develop an efficient electrochemical reforming of CH_4/CO_2 to produce syngas in an SOE; the schematic of the process is shown in Fig. 1. We use redox-stable perovskite LSCM both as cathode and anode, whereas the $Ni_{1-x}Cu_x$ alloy nanocatalysts are grown in situ on an LSCM scaffold to exsolve anchored and confined interface architecture. The strong metal/oxide interface interactions would deliver enhanced high-temperature stability and coking resistance. Chemical activation of CO_2 and carbon coking resistance are investigated on these exsolved interfaces as well as their effectiveness for the efficient electrochemical reforming of CH_4/CO_2 to produce syngas.

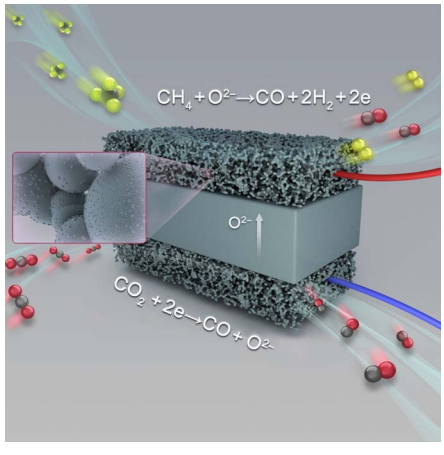

Fig. 1. The schematic of electrochemical CO_2/CH_4 reforming process in an SOE to produce syngas; CO_2 electrolysis is performed in the cathode, whereas electrochemical oxidation of CH_4 is performed in the anode.

RESULTS AND DISCUSSION

Figure 2A shows the x-ray diffraction (XRD) of Ni/Cu co-doped LSCM that are denoted as $(La_{0.75}Sr_{0.25})_{0.9}(Cr_{0.5}Mn_{0.5})_{0.9}(Ni_{1-x}Cu_x)_{0.1}O_{3-\delta}$ (LSCM-$Ni_{1-x}Cu_x$) in oxidation state. The doping of metal in the host lattice would transform Ni/Cu into a metallic alloy nanocatalyst on LSCM scaffold after reduction, whereas the A-site deficiency in perovskite LSCM would facilitate the exsolution of metal nanoparticles. As expected, the Ni/Cu are exclusively present as Ni^{2+} and Cu^{2+}, as shown in the x-ray photoelectron spectroscopy (XPS) images in fig. S1, indicating the successful doping in the host lattice. Figure 2B shows the XRD of LSCM-$Ni_{1-x}Cu_x$ in a reduced state, which reveals the presence of $Ni_{1-x}Cu_x$ alloy phase upon reduction. XPS in fig. S1 confirms that only metallic Ni/Cu is observed upon reduction, which further validates the transformation of Ni^{2+} and Cu^{2+} into a metallic $Ni_{1-x}Cu_x$ alloy. The oxygen storage capacity of LSCM is around 0.09 mol in the redox cycle, whereas the oxygen storage capacity is up to 0.18 mol for LSCM-$Ni_{1-x}Cu_x$ as shown in fig. S2A, which implies that up to 90% of Ni/Cu dopants have been exsolved on LSCM scaffold upon reduction. Figure 2C shows the scanning electron microscopy (SEM) graph of LSCM particles after reduction, which displays the uniform $Ni_{0.5}Cu_{0.5}$ nanoparticles anchoring the LSCM scaffold surface. The metallic alloy nanoparticles exist within a narrow size distribution, with an average of 40 nm, which should deliver highly active exsolved interfaces at the nanoscale. Figure 2D shows that the grown $Ni_{0.5}Cu_{0.5}$ nanoparticles deeply anchor on the LSCM substrate according to HRTEM (high-resolution transmission electron microscopy) observations, which demonstrates a clear heterojunction between the two phases that is anticipated to produce a strong interaction at exsolved interfaces. In addition, the anchoring effect should provide enhanced thermal stability against the severe long-term agglomeration, whereas the nanoparticle regeneration is also possible through periodic redox cycling. The exsolution of confined interfaces is a generic approach that is expected to be extended to many more scaffolds by synergistic control of doping and nonstoichiometry. Other substrates like ceria and nickel can be doped into lattice to form a $Ce_{1-x}Ni_xO_{2-\delta}$ solid solution, and then the nickel nanoparticles can be grown in situ on the ceria surface after reduction at high temperatures.

The growth of metal nanoparticles on the LSCM scaffold further improves the mixed conductivity in a reducing atmosphere in fig. S2B. The exsolved interfaces are expected to have enhanced catalytic activity, whereas the LSCM with oxygen nonstoichiometry may facilitate chemical CO_2 adsorption/activation at high temperatures. Figure 3A shows the chemical adsorption of CO_2 at 800°C in the in situ Fourier transform infrared (FTIR) test, which demonstrates the effective chemical adsorption/activation of CO_2 as confirmed by the transition state (TS) between the CO_2 molecule and the carbonate ion (*19*, *20*). With the exsolved interfaces, significant enhancement of chemical adsorption/activation of CO_2 would be anticipated on the tailored LSCM scaffold. Theoretical calculations were tentatively performed to provide mechanistic insights into the CO_2 adsorption onto M/LCO (001) surfaces, where M represents the Cu, Ni metal, and Ni-Cu alloy, whereas LCO denotes a simplified $LaCrO_3$ substrate. The possible configurations for the most stable adsorption are shown in fig. S3 (A to C), whereas other configurations are shown in fig. S4. Most of these adsorption configurations involve CO_2 forming a bidentate. The chemisorption on (Ni-Cu)/LCO demonstrates an adsorption energy of −2.45 eV, which is significantly higher than that for the Cu (−0.94 eV) and Ni (−1.96 eV) cluster, indicating a favorable alloy effect for CO_2 adsorption. An overview of adsorption energies, bond

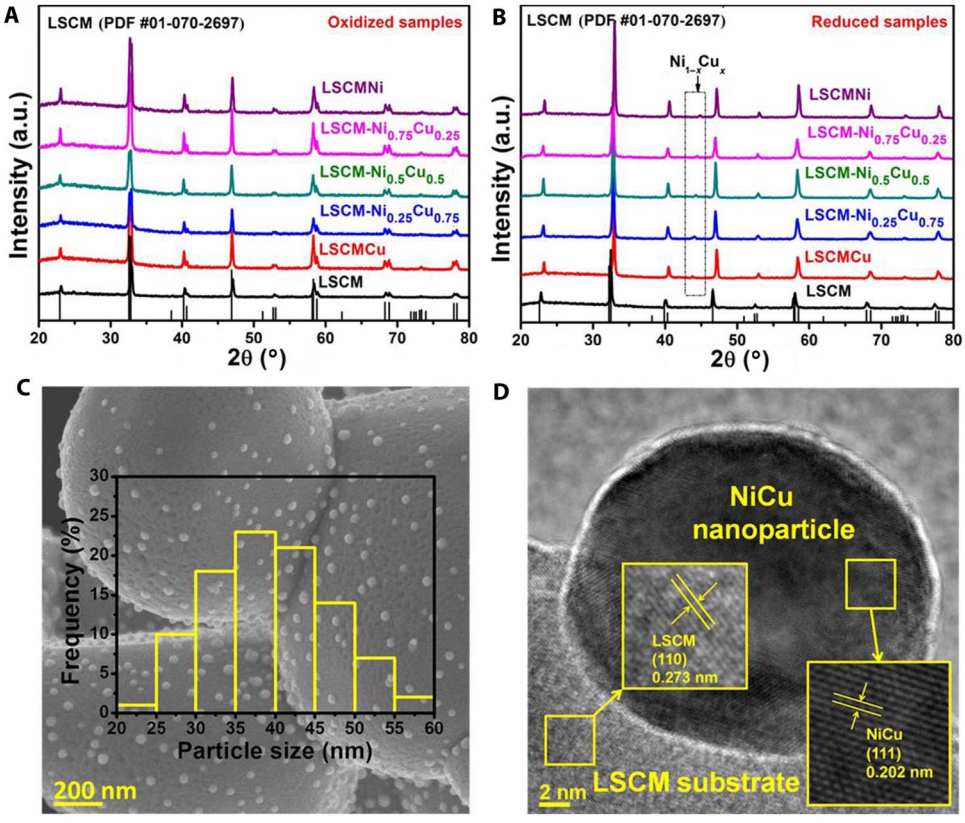

Fig. 2. XRD patterns and microstructure of samples. (**A** and **B**) XRD of the oxidized samples (A) and reduced samples (B), respectively. a.u., arbitrary units; PDF, powder diffraction file. (**C**) SEM image of the reduced LSCM-$Ni_{0.5}Cu_{0.5}$. (**D**) Transmission electron microscopy (TEM) microscopic results of the reduced LSCM-$Ni_{0.5}Cu_{0.5}$.

distances, and angles is provided in table S1. In all (Ni-Cu)/LCO systems, the O atom of CO_2 binds with the surface Cr atom, whereas the C atom binds with the Ni atom. The Ni-C distances are in the range of 1.88 to 2.04 Å. The elongated C–O bonds and bent O–C–O angles in CO_2 additionally suggest significant activation upon adsorption. On the other hand, we consider the possible effect of oxygen vacancy on CO_2 activation at the interfaces. We considered one oxygen vacancy at the interface (fig. S5, A to C) and found that the adsorption energy of (Ni-Cu)/LCO is significantly enhanced to −2.72 eV as shown in Fig. 3B. The synergistic effect of the Ni-Cu alloy and oxygen vacancy facilitates the adsorption of CO_2 at interfaces. The contour plots in fig. S3H show that the charge density changes mainly emerge in the 2p orbitals of the C and O1 atoms of CO_2, the Cu atom, and the relevant surface Cr atoms. The C atom of the CO_2 and the O2 atom gain the electrons, O1 also receives some electron density, donated by all the surrounding atoms, and the Cr atoms of the LCO surface and the Cu atom of the Ni-Cu clusters lose the electrons, which means the charge transfers from the interface to CO_2. To sum up, the Ni-Cu cluster and surface defect with oxygen vacancy on the (Ni-Cu)/LCO interface system would compose an active interface structure, which greatly promotes the chemical adsorption of CO_2. As mentioned above, CO_2 bending upon chemisorption suggests electrons transfer from the interface to the CO_2 moiety. As shown in table S1, most of the charges are transferred toward the carbon atom. The charge transfer in the alloy is more favorable, which indicates that the alloy tends to have stronger interaction with CO_2, that is, more electrons are transferred from the interface to the CO_2; thus, the binding of CO_2 will be stronger. To validate the density functional theory (DFT) calculation for mimicking the surface adsorption behavior at high temperatures, we further conducted the molecular dynamics simulation at 300 to 1100 K to understand the chemisorption of CO_2 at interfaces at high temperatures. As shown in fig. S5 (D to L), the chemisorption of CO_2 at the (Ni-Cu)/LCO (001) system surface is still stable even at 300 to 1100 K, which further indicates that the chemisorption of CO_2 is pretty strong at the exsolved interface architectures. The chemical adsorption/activation of CO_2 at interfaces is expected to significantly enhance electrode activity.

Long-term stability of nanocatalysts at high temperatures remains a major challenge due to nanoparticle agglomeration leading to performance degradation. Here, the nickel-copper catalyst is exsolved and anchored on the LSCM scaffold as shown in Fig. 2C, which should deliver enhanced high-temperature stability against nanoparticle agglomeration. For the reforming of CH_4/CO_2 at high temperatures, carbon deposition causes severe deactivation of nickel catalysts, which mainly originates from CO disproportionation and CH_4 pyrolysis. As shown in Fig. 3C, the LSCM scaffold with in situ–grown and anchored $Ni_{0.5}Cu_{0.5}$ alloy nanoparticles demonstrates remarkable coking resistance in the H_2/CH_4 mixture at 800°C for 3 hours. Only a little amount of carbon is present at the exsolved interfaces. However, serious carbon deposition is inevitable if metal nanoparticles are simply loaded on the scaffold as shown in the inset image in Fig. 3C. One reason may be the strong interactions at the exsolved interfaces at nanoscale that enhance coking resistance of the nickel nanocatalyst, which is probably due to the charge transferred from metal

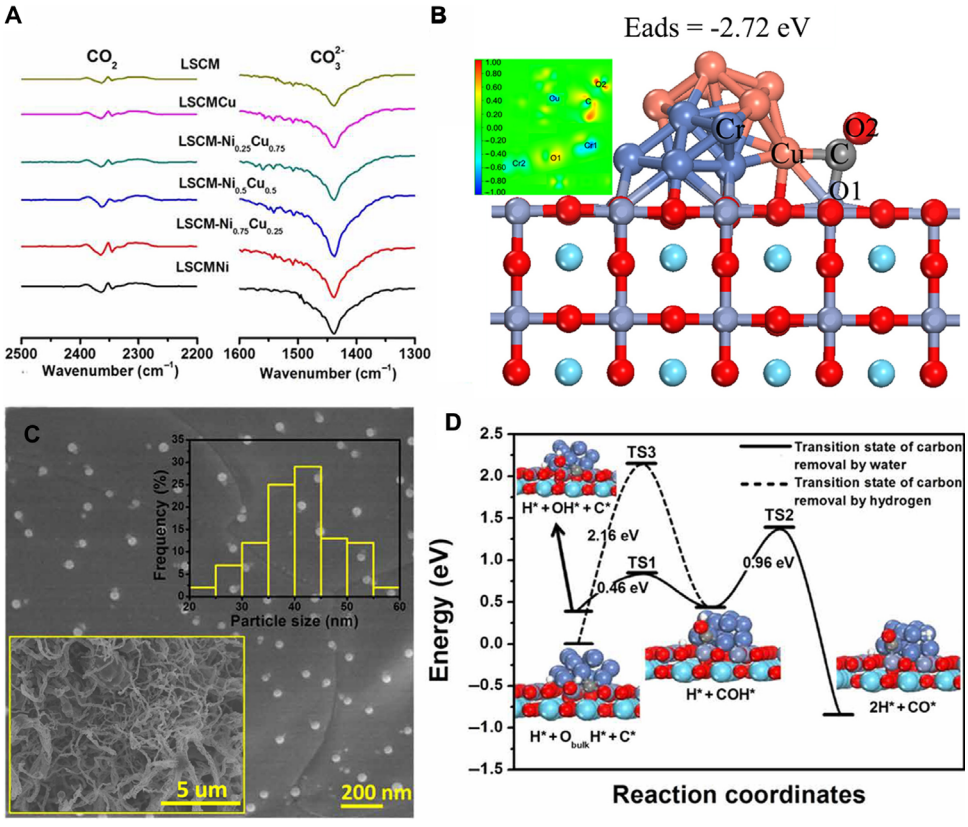

Fig. 3. The performance of CO_2 adsorption and coking resistance. (**A**) In situ FTIR spectroscopy of CO_2 for a series of samples at 800°C. (**B**) The most stable adsorption configurations of CO_2 on the defected site of the (Ni-Cu)/LCO (001) system surface. (**C**) Carbon coking resistance of LSCM-$Ni_{0.5}Cu_{0.5}$ with a flow of 20% CH_4/H_2 at 800°C for 4 hours. (**D**) TS of carbon removal. The energies for removal of chemisorbed carbon species on Ni/LCO (001) are relative to the dissociation of hydrogen on the Ni/LCO (001) interface. Asterisk denotes an adsorbed species on the Ni/LCO (001) surface.

particles with strong interface interactions. Another reason would be the alloy effects with strong interactions that can also enhance coking resistance (*15*). In a real reforming process, we normally consider the feasibility of carbon removal to evaluate the coking resistance performance. Here, we constructed a Ni/LCO (001) model with oxygen vacancies at the interface to investigate the mechanism of carbon removal in the presence of H_2 or H_2O. According to previous studies (*21*, *22*), H_2O prefers to dissociate at the metal/oxide interface compared to metal and oxide surfaces. It is found that H_2O is strongly adsorbed on Cr atoms at the interface, which releases an energy of −1.94 eV and leads to a barrier less than the O–H bond cleavage. The dissociated OH then reacts with an adsorbed C on the Ni/LCO (001) interface via TS1 (reaction barrier, 0.46 eV) to form an intermediate COH, which is subsequently dissociated to CO and H via TS2 (reaction barrier, 0.96 eV) as shown in Fig. 3D. Because the reaction is carried out at a constant high temperature of 800°C, the possibility of carbon removal induced by H_2 was also considered. The results show that the H_2 molecules overcome the energy barrier dissociation of 1.05 eV, and then the dissociated H atom is adsorbed on the O atom near the interface. After the adsorption of the H atom, it will take out the O atom in LCO and form OH. The OH reacts with C via TS3 (reaction barrier, 2.16 eV) to form COH and then subsequently dissociates to CO, which is the same as the case of carbon removal induced by H_2O. Therefore, the system has a strong resistance to carbon deposition at high temperatures because of the synergistic effect of these two processes. In addition, the carbon removal at the interfaces is highly favorable with electrochemically provided oxygen species in the anode because the oxygen ion is simultaneously transported from the cathode under external applied voltages, which would electrochemically oxidize the deposited carbon into carbon monoxide gas and further substantially enhance coking resistance.

Single solid oxide cells with porous LSCM electrode decorated with nanoscale metal catalysts were constructed, respectively, and the cell microstructures are shown in fig. S6. To evaluate the electrode performance, the electrolysis of CO_2 was initially performed with the tailored LSCM cathode and the $(La_{0.8}Sr_{0.2})_{0.95}MnO_{3-\delta}$ (LSM) anode at 800°C. Figure 4 (A and B) shows that the current-voltage (*I-V*) relationship reveals the superior performance with up to 300% enhancement of the LSCM cathodes with exsolved interfaces in comparison to the bare LSCM cathode. The growth of metal nanoparticles drastically improves the current density to 1.2 A cm^{-2} at 1.5 V when optimum alloy compositions are obtained. These values are comparable to the performances of nickel-decorated $(La,Sr)(Ti,Mn)O_{3+\delta}$ cathodes and $La_{0.43}Ca_{0.37}Ni_{0.06}Ti_{0.94}O_{3+\delta}$ prepared with an electrochemical switching method (*14*, *23*). The in situ impedance spectra in fig. S7 show the electrode polarization resistance is as low as 0.3 ohm·cm^2 for the $Ni_{0.5}Cu_{0.5}$-decorated LSCM, indicating the remarkable enhancement of electrode activity (*24*). The polarization resistance of electrodes gradually decreases with increasing nickel content in $Ni_{1-x}Cu_x$ alloy nanoparticles when compared with all of the proportions, which

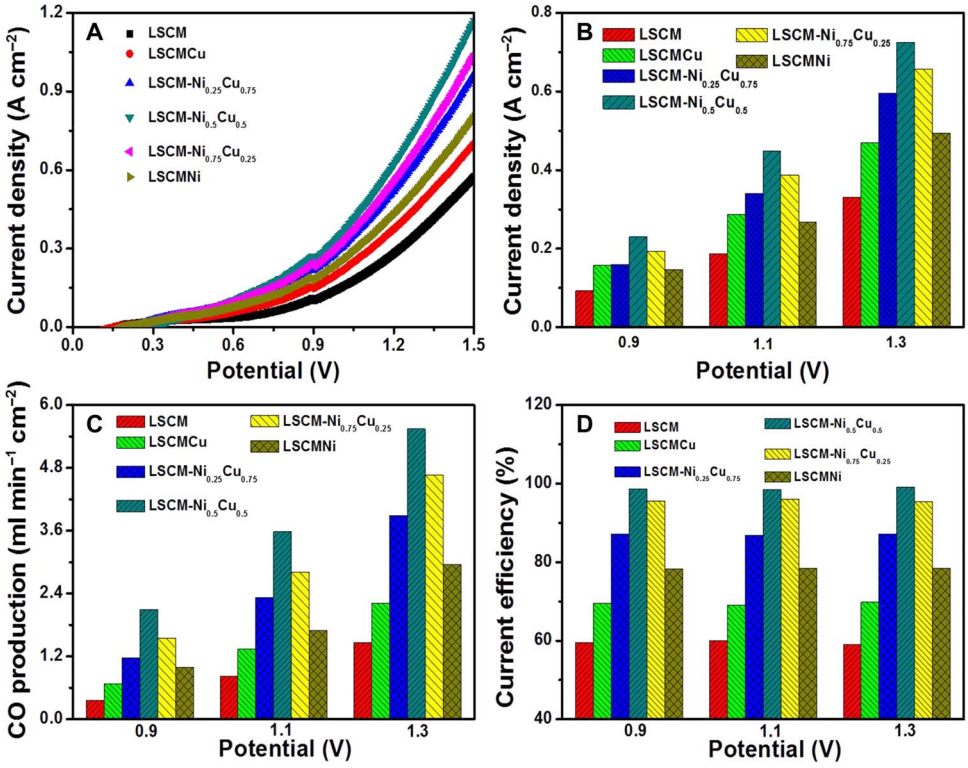

Fig. 4. The performances of CO_2 electrolysis. (**A**) The *I-V* curves of the electrolysers based on different cathode materials for CO_2 electrolysis at 800°C. (**B**) The short-term performances of CO_2 electrolysis at different applied voltages. (**C** and **D**) CO production (C) and current efficiencies (D) with various cathode materials.

is attributed to the catalytic activity of nickel metal being greater than that of copper. The catalytic activity of the electrode with exsolved interfaces can be continuously tuned according to the strong dependence of the electrode activity on the $Ni_{1-x}Cu_x$ alloy compositions under reducing atmospheres at high temperatures, whereas the optimum synergetic effect is observed for the $Ni_{0.5}Cu_{0.5}$ composition. Figure 4 (C and D) shows the CO generation rate and current efficiency, respectively, which again confirms that the synergy of interface catalysis and alloy effect delivers the best performances with current efficiency up to 100%. Figure 5 (A and B) shows the *I-V* curves of the SOEs with CO_2 electrolysis in the $Ni_{0.5}Cu_{0.5}$-LSCM cathode and CH_4 oxidation in different anodes. The electrochemical oxidation of CH_4 shows a strong dependence on the $Ni_{1-x}Cu_x$ composition in the interface architectures, in which the current density also increases rapidly with increasing nickel content up to 50% because of the high catalytic activity of nickel. Thus, a high content of nickel catalyst improves the interface catalysis. However, an optimum composition of $Ni_{0.5}Cu_{0.5}$ has been proven to be highly effective to enhance electrochemical performance. It is observed that the current density for CH_4 oxidation has been significantly enhanced by ~100% in contrast to the performances only for CO_2 electrolysis. The voltage is accordingly reduced by 0.1 to 0.2 V at identical current densities when the electrochemical oxidation of CH_4 is performed in the anode in conjunction with CO_2 electrolysis in the cathode. This further indicates that the electrochemical reforming of CH_4/CO_2 is more efficient than CO_2 electrolysis because the CH_4 atmosphere in the anode remarkably reduces oxygen partial pressure that accordingly facilitates the whole electrochemical process. In situ impedance tests as shown in Fig. 5C and fig. S8 further confirm that the electrode polarization resistance is significantly reduced by 30% in contrast to the CO_2 electrolysis under identical operation conditions. Figure 5D shows the generation of H_2/CO in the anode in relation to different $Ni_{1-x}Cu_x$ compositions and applied voltages. The H_2/CO production demonstrates a strong dependence on $Ni_{1-x}Cu_x$ compositions in the anode, where the best performances are observed for the $Cu_{0.5}Ni_{0.5}$-LSCM anode, which indicates that the optimum alloy composition delivers the best enhanced activity for electrochemical oxidation of CH_4 in the anode. In addition, the H_2/CO ratio shows a dependence on the applied voltages with an optimum ratio of 2 below 1.1 V; however, a ratio below 2 is observed at higher voltages, indicating the tendency of selective oxidation of CO in H_2/CO mixtures at high voltages that decreases CO concentration in contrast to H_2. In this simultaneous process, the conversion ratio of CO_2/CH_4 would rely on both the gas flow rates and the passing current densities, whereas up to 90% conversion ratios can be obtained without obvious carbon deposition from the CO disproportionation and CH_4 pyrolysis. Here, syngas is the main product, but ethylene is ~500 parts per million, which also confirms the possibility of direct generation of ethylene. If in situ catalysis is combined with the electrochemical process on a porous electrode in a single step, then the CO_2/CH_4 would be further directly converted into chemicals such as ethylene when the exsolved interfaces with iron nanoparticles were used to better suit the in situ catalysis process. Figure S9 shows the short-term performance of the electrochemical reforming of CH_4/CO_2 with the $Cu_{0.5}Ni_{0.5}$-LSCM electrode in a symmetric cell, which indicates remarkable stability even after 300 hours of high-temperature operation. The all-perovskite symmetric cell demonstrates excellent redox stability even after 10 redox cycles within the frames of these experiments. The exsolution of anchored metal/oxide interfaces to

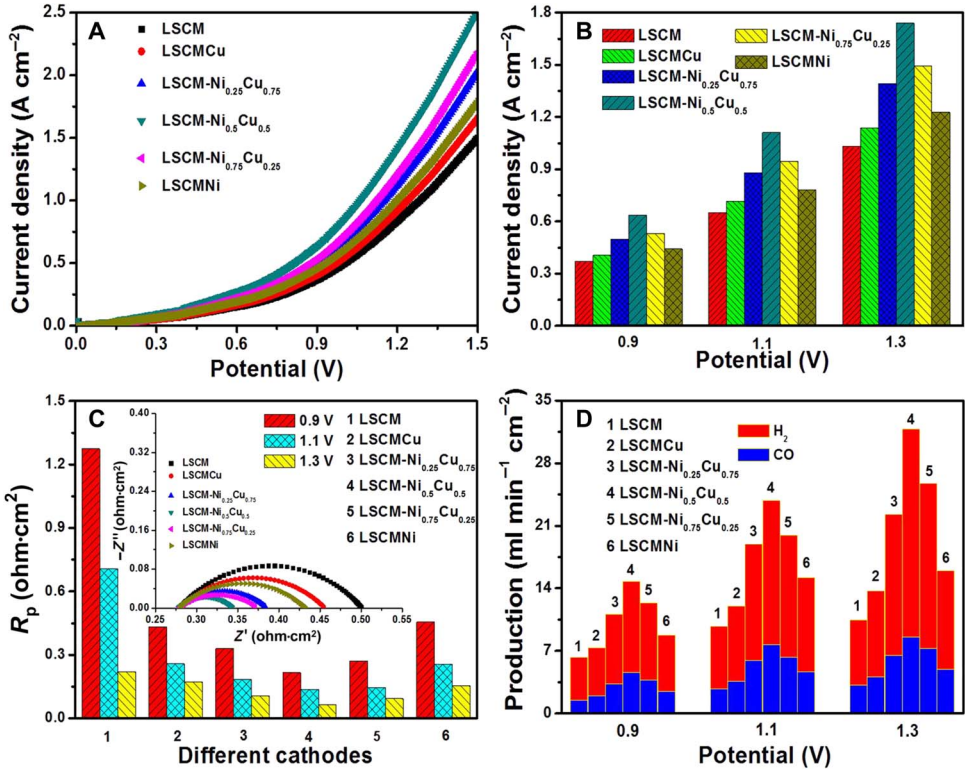

Fig. 5. The performances of the electrochemical reforming of CH_4/CO_2. (**A**) The *I-V* curves of the CO_2 electrolysis with simultaneous electrochemical oxidation of CH_4 electrolysers based on different anode materials at 800°C. (**B**) The short-term performances of the electrochemical reforming of CH_4/CO_2 at different applied voltages. (**C**) In situ ac impedance spectroscopy with different anodes at different applied voltages. R_p, polarization resistance. (**D**) CO production and H_2 production in anode with various anode materials.

the perovskite lattice at nanoscale is expected to improve both long-term and redox stability by preventing particle coalescence driven by surface energy reduction.

CONCLUSION

In conclusion, we have demonstrated a highly efficient electrochemical reforming of CH_4/CO_2 in an all-perovskite SOE with exceptionally high performance and stability. The exsolved metal/oxide interfaces at nanoscale show strong interactions that deliver enhanced coking resistance and stability. These confined metal/oxide interface architectures enable both carbon removal performance and high-temperature chemical CO_2 adsorption/activation. In addition, our work furthermore exhibits high-temperature stability for 300 hours with significant redox cycling ability, providing the tools to develop an alternative route for CO_2/CH_4 conversion for energy conversion and storage.

MATERIALS AND METHODS

Synthesis

LSCM and $(La_{0.75}Sr_{0.25})_{0.9}(Cr_{0.5}Mn_{0.5})_{0.9}(Ni_xCu_{1-x})_{0.1}O_{3-\delta}$ [LSCMNi, x = 1.0; LSCM-$Ni_{0.75}Cu_{0.25}$, x = 0.75; LSCM-$Ni_{0.5}Cu_{0.5}$, x = 0.5; LSCM-$Ni_{0.25}Cu_{0.75}$, x = 0.25; LSCMCu, x = 0] were synthesized using a glycine-nitrate combustion method (*25*, *26*). The collected powders were sintered at 1200°C for 5 hours with a heating rate of 3°C min^{-1} in air. The LSM and $Ce_{0.8}Sm_{0.2}O_{2-\delta}$ (SDC) powders were prepared using a combustion method, whereas the corresponding heat treatments were at 1100°C for 3 hours and at 800°C for 3 hours, respectively (*9*, *27*). The pure LSCM, LSCMNi, LSCM-$Ni_{0.75}Cu_{0.25}$, LSCM-$Ni_{0.5}Cu_{0.5}$, LSCM-$Ni_{0.25}Cu_{0.75}$, and LSCMCu powders were treated in 5% H_2/Ar at 800°C for 20 hours to prepare the reduced samples. $La_{0.9}Sr_{0.1}Ga_{0.8}Mg_{0.2}O_3$ (LSGM) was prepared using a solid-state reaction method and then pressed into pellet and sintered at 1500°C for 6 hours in air (*28*). The LSGM disk with a thickness of 0.6 mm and a diameter of 20 mm was polished and used as an electrolyte support.

Characterization

The crystal structures of the samples were characterized by XRD with a scan rate of 5°C min^{-1} in the 2θ range of 20° to 80°. XPS with a Al Kα (1486.6 eV) radiation source was carried out to analyze the elemental states of the samples. A dc four-terminal method was used to investigate the conductivity of the samples in 5% H_2/Ar over a temperature range of 600° to 800°C. A thermogravimetric analysis method was used to analyze the oxygen stoichiometry of the samples. SEM was used to investigate the sample microstructure. TEM analysis with selected-area diffraction was performed to observe the interface architecture on a JEOL 2100F field emission transmission electron microscope operated at 200 kV.

Electrochemical characterization

The cells with LSGM electrolyte were fabricated using different electrodes (0.5 cm^2) and the SDC at the ratio of 35 weight % (wt %) and proper amount of α-terpineol with cellulose were added. The electrode slurries were screen-printed on both surfaces of the LSGM disk, followed by a heat treatment at 1100°C for 3 hours to assemble a single

cell. The gold mesh (82 mesh) was used as current collector, and the gold wire is 0.06 mm in diameter. The electrodes were prereduced using 5% H_2/Ar for activation at 800°C. For the electrochemical tests, an electrochemical working station (IM6, Zahner) in a two-electrode mode was used. The compositions of the cycling gas products were analyzed using an online gas chromatography (GC2014, Shimazu). In situ impedance data were recorded with a voltage amplitude of 10 mV over the applied frequency in the range of 0.1 Hz to 4 MHz. Long-term stability tests were performed at a fixed voltage while the current densities were recorded online using an electrochemical working station.

Theoretical calculations

DFT calculations were performed using a plane wave basis set Vienna Ab initio Simulation Package code (*29*). Within the projector augmented wave framework, the plane wave cutoff used for total energy calculations was set to 450 eV. The generalized gradient approach was used including the Perdew-Burke-Ernzerhof functional to describe exchange and correlation (*30*). The energies and residual forces were converged to 10^{-6} eV and 0.02 eV $Å^{-1}$, respectively. The optimized crystal structure and lattice parameters of LCO($LaCrO_3$) on a 3 × 3 × 6 *k*-point grid was cubic, with a = 3.891 Å, which is in good agreement with the experimental values (*31*). A p(2 × 2) superstructure with four layers (160 atoms) of the (001) surface of LCO was used to simulate the periodic slab model. The two bottom layers were fixed to its bulk geometry during optimization, and other atoms were fully relaxed. The vacuum region is 15 Å thick. The Cu segregation on the (001) surface slab of the LCO was mimicked by a system containing a Cu cluster with 13 Cu atoms laying on the (001) surface of LCO, and Ni clusters were similar to Cu clusters; however, Ni-Cu clusters contained seven Ni atoms and six Cu atoms. A 2 × 2 × 1 *k*-point grid was used for Brillouin zone sampling of the M(Cu, Ni, or Ni-Cu)/LCO (001) surface system. The adsorption energy of CO_2 was calculated as $E_{ads} = E_{total} - E_{CO_2} - E_{substrate}$, where E_{total} is the total energy of the adsorption system, E_{CO_2} and $E_{substrate}$ are the CO_2 in gas phase and the energy of the M/LCO surface system without adsorption, respectively (*32*). TS searches were carried out by the climbing image nudged elastic band method (*33*, *34*). The stability of the high-temperature structure was verified by molecular dynamics simulation.

SUPPLEMENTARY MATERIALS

Supplementary material for this article is available at http://advances.sciencemag.org/cgi/content/full/4/3/eaar5100/DC1

fig. S1. XPS results of oxidized and reduced samples.
fig. S2. Thermogravimetric analysis (TGA) of reduced samples and the conductivities of reduced samples.
fig. S3. The best configurations for chemisorption of CO_2 on system surface and corresponding differential charge density.
fig. S4. Different configurations for chemisorption of CO_2 on the M/LCO (001) system surface.
fig. S5. The configurations for chemisorption of CO_2 on the M/LCO (001) system defected surface and the corresponding molecular dynamics calculation.
fig. S6. SEM image for the single cells.
fig. S7. The ac impedance spectra of the electrolyzers.
fig. S8. The ac impedance spectra of the electrolyzers for single solid oxide cells.
fig. S9. The long-term and redox cycling performance of the symmetric cell.
table S1. The adsorption energies, bond distances, and bond angle after CO_2 adsorption and charge analysis of a partial system.

REFERENCES AND NOTES

1. D. Pakhare, J. Spivey, A review of dry (CO_2) reforming of methane over noble metal catalysts. *Chem. Soc. Rev.* **43**, 7813–7837 (2014).
2. A. G. Bhavani, W. Y. Kim, J. S. Lee, Barium substituted lanthanum manganite perovskite for CO_2 reforming of methane. *ACS Catal.* **3**, 1537–1544 (2013).
3. K. Mette, S. Kühl, A. Tarasov, M. G. Willinger, J. Kröhnert, S. Wrabetz, A. Trunschke, M. Scherzer, F. Girgsdies, H. Düdder, K. Kähler, K. F. Ortega, M. Muhler, R. Schlögl, M. Behrens, T. Lunkenbein, High-temperature stable Ni nanoparticles for the dry reforming of methane. *ACS Catal.* **6**, 7238–7248 (2016).
4. Z. Li, L. Mo, Y. Kathiraser, S. Kawi, Yolk–Satellite–Shell structured Ni–Yolk@Ni@SiO_2 nanocomposite: Superb catalyst toward methane CO_2 reforming reaction. *ACS Catal.* **4**, 1526–1536 (2014).
5. F. Polo-Garzon, D. Pakhare, J. J. Spivey, D. A. Bruce, Dry reforming of methane on Rh-doped pyrochlore catalysts: A steady-state isotopic transient kinetic study. *ACS Catal.* **6**, 3826–3833 (2016).
6. S. D. Ebbesen, S. H. Jensen, A. Hauch, M. B. Mogensen, High temperature electrolysis in alkaline cells, solid proton conducting cells, and solid oxide cells. *Chem. Rev.* **114**, 10697–10734 (2014).
7. K. Xie, Y. Zhang, G. Meng, J. T. S. Irvine, Direct synthesis of methane from CO_2/H_2O in an oxygen-ion conducting solid oxide electrolyser. *Energ. Environ. Sci.* **4**, 2218–2222 (2011).
8. C. Jiang, J. Ma, A. D. Bonaccorso, J. T. S. Irvine, Demonstration of high power, direct conversion of waste-derived carbon in a hybrid direct carbon fuel cell. *Energ. Environ. Sci.* **5**, 6973–6980 (2012).
9. C. Ruan, K. Xie, A redox-stable chromate cathode decorated with in situ grown nickel nanocatalyst for efficient carbon dioxide electrolysis. *Cat. Sci. Technol.* **5**, 1929–1940 (2015).
10. S. Tao, J. T. S. Irvine, A redox-stable efficient anode for solid-oxide fuel cells. *Nat. Mater.* **2**, 320–323 (2003).
11. C. Zhu, L. Hou, S. Li, L. Gan, K. Xie, Efficient carbon dioxide electrolysis with metal nanoparticles loaded $La_{0.75}Sr_{0.25}Cr_{0.5}Mn_{0.5}O_{3-\delta}$ cathodes. *J. Power Sources* **363**, 177–184 (2017).
12. S. Boulfrad, M. Cassidy, J. T. S. Irvine, Adhesion and percolation parameters in two dimensional Pd–LSCM composites for SOFC anode current collection. *Adv. Funct. Mater.* **20**, 861–866 (2010).
13. J. Ni, L. Chen, J. Lin, S. Kawi, Carbon deposition on borated alumina supported nano-sized Ni catalysts for dry reforming of CH_4. *Nano Energy* **1**, 674–686 (2012).
14. L. Ye, M. Zhang, P. Huang, G. Guo, M. Hong, C. Li, J. T. S. Irvine, K. Xie, Enhancing CO_2 electrolysis through synergistic control of non-stoichiometry and doping to tune cathode surface structures. *Nat. Commun.* **8**, 14785 (2017).
15. S. A. Theofanidis, V. V. Galvita, H. Poelman, G. B. Marin, Enhanced carbon-resistant dry reforming Fe-Ni catalyst: Role of Fe. *ACS Catal.* **5**, 3028–3039 (2015).
16. M. Khzouz, J. Wood, B. Pollet, W. Bujalski, Characterization and activity test of commercial Ni/Al_2O_3, Cu/ZnO/Al_2O_3 and prepared Ni–Cu/Al_2O_3 catalysts for hydrogen production from methane and methanol fuels. *Int. J. Hydrogen Energy* **38**, 1664–1675 (2013).
17. X. Meng, X. Gong, N. Yang, Y. Yin, X. Tan, Z.-F. Ma, Carbon-resistant Ni-YSZ/Cu–CeO_2-YSZ dual-layer hollow fiber anode for micro tubular solid oxide fuel cell. *Int. J. Hydrogen Energy* **39**, 3879–3886 (2014).
18. H. Wei, K. Xie, J. Zhang, Y. Zhang, Y. Wang, Y. Qin, J. Cui, J. Yan, Y. Wu, In situ growth of Ni_xCu_{1-x} alloy nanocatalysts on redox-reversible rutile (Nb,Ti)O_4 towards high-temperature carbon dioxide electrolysis. *Sci. Rep.* **4**, 5156 (2014).
19. M. C. Figueiredo, I. Ledezma-Yanez, M. T. M. Koper, In situ spectroscopic study of CO_2 electroreduction at copper electrodes in acetonitrile. *ACS Catal.* **6**, 2382–2392 (2016).
20. T. Ishihara, N. Jirathiwathanakul, H. Zhong, Intermediate temperature solid oxide electrolysis cell using $LaGaO_3$ based perovskite electrolyte. *Energ. Environ. Sci.* **3**, 665–672 (2010).
21. J. A. Rodriguez, S. Ma, P. Liu, J. Hrbek, J. Evans, M. Pérez, Activity of CeO_x and TiO_x nanoparticles grown on Au(111) in the water-gas shift reaction. *Science* **318**, 1757–1760 (2007).
22. L. Yang, Y. Choi, W. Qin, H. Chen, K. Blinn, M. Liu, P. Liu, J. Bai, T. A. Tyson, M. Liu, Promotion of water-mediated carbon removal by nanostructured barium oxide/nickel interfaces in solid oxide fuel cells. *Nat. Commun.* **2**, 357 (2011).
23. J.-h. Myung, D. Neagu, D. N. Miller, J. T. S. Irvine, Switching on electrocatalytic activity in solid oxide cells. *Nature* **537**, 528–531 (2016).
24. C. Yang, Z. Yang, C. Jin, G. Xiao, F. Chen, M. Han, Sulfur-tolerant redox-reversible anode material for direct hydrocarbon solid oxide fuel cells. *Adv. Mater.* **24**, 1439–1443 (2012).
25. D. M. Bastidas, S. Tao, J. T. S. Irvine, A symmetrical solid oxide fuel cell demonstrating redox stable perovskite electrodes. *J. Mater. Chem.* **16**, 1603–1605 (2006).
26. L. Shi, C. Zeng, Y. Jin, T. Wang, N. Tsubaki, A sol–gel auto-combustion method to prepare Cu/ZnO catalysts for low-temperature methanol synthesis. *Cat. Sci. Technol.* **2**, 2569–2577 (2012).
27. G.-B. Jung, T.-J. Huang, Sintering temperature, microstructure and resistivity of polycrystalline $Sm_{0.2}Ce_{0.8}O_{1.9}$ as SOFC's electrolyte. *J. Mater. Sci.* **38**, 2461–2468 (2003).

28. T. Ishihara, M. Honda, T. Shibayama, H. Furutani, Y. Takita, An intermediate temperature solid oxide fuel cell utilizing superior oxide ion conducting electrolyte, doubly doped $LaGaO_3$ perovskite. *Ionics* **4**, 395–402 (1998).
29. W. Yang, Z. Wang, Z. Wang, Z. Yang, C. Xia, R. Peng, X. Wu, Y. Lu, Enhanced catalytic activity toward O_2 reduction on Pt-modified $La_{1-x}Sr_xCo_{1-y}Fe_yO_{3-\delta}$ cathode: A combination study of first-principles calculation and experiment. *ACS Appl. Mater. Interfaces* **6**, 21051–21059 (2014).
30. F. Han, Y. Zhu, X. He, Y. Mo, C. Wang, Electrochemical stability of $Li_{10}GeP_2S_{12}$ and $Li_7La_3Zr_2O_{12}$ solid electrolytes. *Adv. Energy Mater.* **6**, 1501590 (2016).
31. A. Wold, R. Ward, Perowskite-type oxides of cobalt, chromium and vanadium with some rare earth elements. *J. Am. Chem. Soc.* **76**, 1029–1030 (1954).
32. Z. Wang, R. Peng, W. Zhang, X. Wu, C. Xia, Y. Lu, Oxygen reduction and transport on the $La_{1-x}Sr_xCo_{1-y}Fe_yO_{3-\delta}$ cathode in solid oxide fuel cells: A first-principles study. *J. Mater. Chem. A* **1**, 12932–12940 (2013).
33. A. Ulitsky, R. Elber, A new technique to calculate steepest descent paths in flexible polyatomic systems. *J. Chem. Phys.* **92**, 1510–1511 (1990).
34. G. Henkelman, B. P. Uberuaga, H. Jónsson, A climbing image nudged elastic band method for finding saddle points and minimum energy paths. *J. Chem. Phys.* **113**, 9901–9904 (2000).

Acknowledgments

Funding: K.X. acknowledges the Natural Science Foundation of China (91545123), the 100 Talents Program of Fujian Province, and the Natural Science Foundation of Fujian Province (2016J01275) for funding this work. F.C. acknowledges the NSF (1210792) and the National Institute of Clean and Low-Carbon Energy (CF9300160020). **Author contributions:** J.L. and C.Z. conducted the experiments. C.P. and C.L. conducted the first principle calculations. K.X. supervised this work and wrote the manuscript. J.L., C.Z., and C.P. contributed equally to this work. All authors were involved in the data analysis and discussion. **Competing interests:** The authors declare that they have no competing interests. **Data and materials availability:** All data needed to evaluate the conclusions in the paper are present in the paper and/or the Supplementary Materials. Additional data related to this paper may be requested from the authors.

Submitted 16 November 2017
Accepted 13 February 2018
Published 30 March 2018
10.1126/sciadv.aar5100

Citation: J. Lu, C. Zhu, C. Pan, W. Lin, J. P. Lemmon, F. Chen, C. Li, K. Xie, Highly efficient electrochemical reforming of CH_4/CO_2 in a solid oxide electrolyser. *Sci. Adv.* **4**, eaar5100 (2018).

ScienceAdvances

Highly efficient electrochemical reforming of CH_4/CO_2 in a solid oxide electrolyser

Jinhai LuChangli ZhuChangchang PanWenlie LinJohn P. LemmonFanglin ChenChunsen LiKui Xie

Sci. Adv., 4 (3), eaar5100. • DOI: 10.1126/sciadv.aar5100

Science Advances (ISSN 2375-2548) is published by the American Association for the Advancement of Science. 1200 New York Avenue NW, Washington, DC 20005. The title *Science Advances* is a registered trademark of AAAS.